Published by IOP Publishing for Sissa Medialab

Received: *May 31, 2022*
Revised: *September 7, 2022*
Accepted: *September 7, 2022*
Published: *September 30, 2022*

Monte Carlo simulations of vehicle-mounted whole-body NaI(Tl) counter

H. Mo,[a] **P. Gong,**[a,b,*] **D. Liang,**[a,b] **Z. Wang,**[a,b] **J. Zhang, Z. Hu,**[a,b] **R. Wu,**[a] **X. Tang,**[a,b] **J. Wang,**[c] **J. Ma**[c] **and X. Yang**[c]

[a] *Department of Nuclear Science and Technology, Nanjing University of Aeronautics and Astronautics, Nanjing 210016, China*
[b] *Key Laboratory of Nuclear Technology Application and Radiation Protection in Astronautics, Ministry of Industry and Information Technology, Nanjing 210016, China*
[c] *Jiangsu Provincial Center for Disease Control and Prevention, Nanjing 210009, China*

E-mail: gongpin@nuaa.edu.cn

Abstract: During a nuclear emergency, an internal exposure detection device with on-site and rapid measurements should be developed to assess the level of internal exposure of people in radioactively contaminated areas. Based on MCNP simulations, this work designed a shielding structure of a NaI(Tl) type vehicle-mounted whole-body counter (VM-WBC) and it has good shielding performance against the background radiation. The mass of the shielding structure was less than 800 kg, and the minimum detectable activity (MDA) of ^{60}Co and ^{137}Cs obtained by simulation for a 10 min measurement was less than 50 Bq. And we also study its counting efficiency calibration by simulating radiation computing phantoms with Chinese and American reference physiological characteristics. Equations that fit counting efficiency, body build index, and photon energy were also developed. The relative efficiency deviation between the equation and the MCNP simulation was less than 5%.

Keywords: Detector modelling and simulations I (interaction of radiation with matter, interaction of photons with matter, interaction of hadrons with matter, etc); Instruments for environmental monitoring, food control and medical use; Simulation methods and programs; Gamma detectors (scintillators, CZT, HPGe, HgI etc)

*Corresponding author.

https://doi.org/10.1088/1748-0221/17/09/P09044

2022 JINST 17 P09044

Contents

1 Introduction

During a nuclear accident, radionuclides released into the environment may get into the human body and cause internal pollution [1]. As an effective internal radioactive pollution detection equipment, the whole-body counter (WBC) is used in many cases for internal radiation detection [2–7]. Because the WBC can qualitatively and quantitatively analyze the types and activities of radionuclides by directly measuring the energy spectrum information of gamma rays emitted from the human body. To reduce the interference of background radiation, the WBC has a very large and heavy shielding structure, and the commercial WBCs from Canberra and Ortec have shields as high as 2–3 m and a weight of 4–6 tons [8, 9]. Such WBCs with large and heavy shielding structures are usually deployed in hospitals, etc., and cannot be moved quickly to the site of a nuclear accident for internal exposure measurements.

To achieve the purpose of quick on-site detection, a vehicle-mounted whole-body counter (VM-WBC) is designed in this study. The VM-WBC has a lightweight shielded structure design, which allows it to be installed on vehicles and to fast reach the site for internal radioactive pollution detection in the event of a nuclear accident. VM-WBC allows evacuees to be tested at the accident site, which improves the efficiency and timeliness of internal contamination detection of evacuees under nuclear accidents. The vehicle model to be adopted in this paper was the IVECO DAILY, a van with a load of about 3.5 tons [10]. Compared with large vehicles, IVECO DAILY has the advantages of lower cost, more compact structure, and flexible driving. However, a not enough mass shielding system will degrade the designed whole-body counter performance.

2022 JINST 17 P09044

2 Design of VM-WBC

2.1 Monte Carlo model

2.1.1 Overall design

Considering the load-bearing capacity of IVECO DAILY, the mass of the detector shielding structure should be less than 1 ton. And the shielding structure should meet the minimum detectable activity (MDA) requirements of the International Commission on Radiological Protection (ICRP) for personal internal exposure detection standards [11]. The vehicle model external view is shown in figure 1(a). Figure 1(b) shows the internal structure of the vehicle, which is divided into an operating room and a testing room by a clapboard.

Figure 1(c) and figure 1(d) show schematic diagrams from different perspectives for the Monte Carlo simulation. The model is composed of the cuboid car body, clapboard, Bottle Manikin Absorber (BOMAB) phantom, and VM-WBC from outside to inside. The MCNP model of VM-WBC consists of a bed, detectors, and a detector shielding structure. The bed is about 1.7 m above the ground, and two $4'' \times 4'' \times 16''$ NaI(Tl) scintillation detectors are located below it. The vehicle used in this study has an internal space of $2\,\text{m} \times 4\,\text{m} \times 2\,\text{m}$. The material of the car body and the clapboard is aluminum alloy. The size of the bed is $1.9\,\text{m} \times 0.7\,\text{m} \times 0.01\,\text{m}$, and it is made of carbon fiber. The phantom in the model is the American National Standard Institute (ANSI) BOMAB phantom [12]. Two sources are used in the MCNP model, which are a soil source and an air source. The soil source is 1.7 m away from the bed. The air source is a cube with a side length of 25 m. In the MCNP code, the center of the air cube is $(0, 0, 0)$, the center of NaI(Tl) is $(50.00\,\text{cm}, -44.10\,\text{cm}, 31.65\,\text{cm})$.

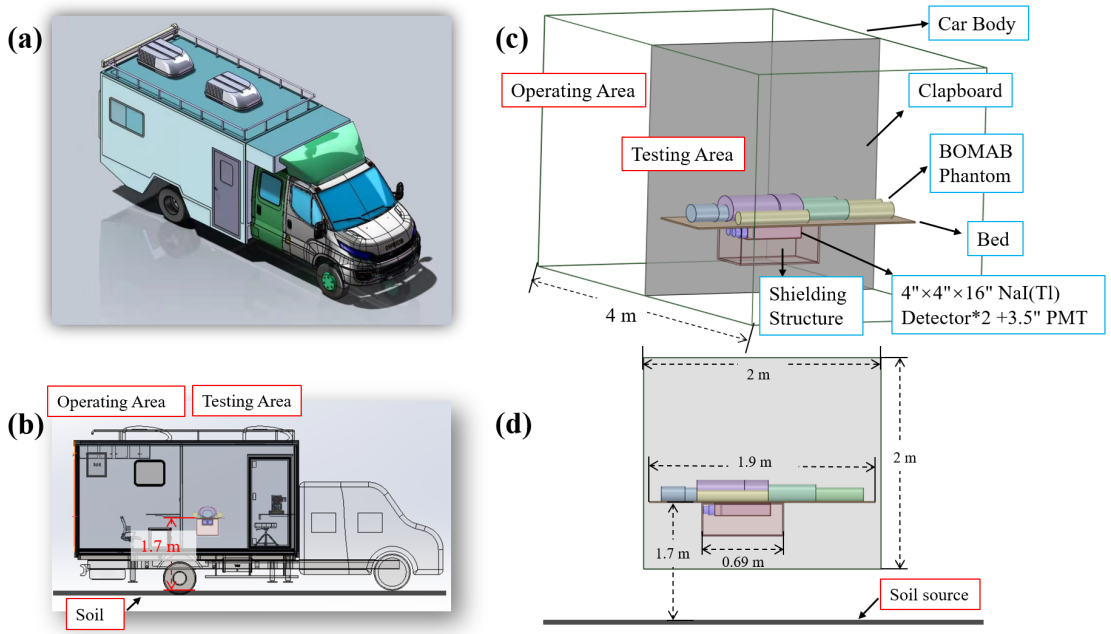

Figure 1. VM-WBC designed in this study: (a) vehicle exterior view; (b) vehicle interior structure diagram; (c) schematic diagram of Monte Carlo model; and (d) front view of Monte Carlo model.

2022 JINST 17 P09044

Since the Monte Carlo code describes static geometry, motion equivalence calculation is needed for objects scanned in motion. The complete scanning process is separated into the sum of discrete steps [13, 14]. VM-WBC requires head-to-toe scanning of evacuees when in use. The entire scanning process is modeled equivalently in a Monte Carlo model by 9 equally spaced detectors, each simulating a 10-minute measurement (figure 2).

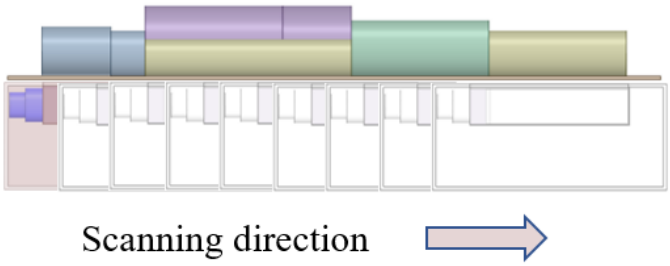

Figure 2. Motion equivalent schematic.

2.1.2 Modeling of the environmental background source

VM-WBC serves the nuclear emergency mission in Jiangsu Province, China. The activity level of the soil background radionuclides in the Monte Carlo model was referred to the data provided by the Jiangsu Provincial Environmental Monitoring Station [15]. The activity concentrations of natural radionuclides ^{238}U, ^{226}Ra, ^{232}Th, ^{40}K were 35.7, 35.8, 49.6, and 568 Bq/kg, respectively. Because natural uranium and thorium decay chains are in long-term radioactive equilibrium in soil. Therefore, the activity of all nuclides in the entire decay chain is the same as that of the parent nucleus.

The radionuclides in soil are mainly due to the decay of uranium-series, thorium-series, and ^{40}K. To take into account the simplicity and accuracy of the source model in the simulation process, in this study, all photon energies in the series decay with a photon intensities greater than 2% were selected for the source setting in the soil background simulation [16, 17]. The specific representative energy and corresponding photon intensities are shown in table 1.

In MCNP simulations, to more precisely obtain the background radiation radiated by the soil in the real environment, a cylindrical soil source is used for simulation. The soil was selected from the elemental composition of classic soils in the world (table 2), and its density was 1.4 g/cm^3 [19].

Determine the maximum dimensions of a cylindrical soil source, including radius and thickness. Assuming the radionuclides are uniformly distributed in the cylinder, the number of source particles per cubic meter of soil remains constant (NPS/m^3 = 3×10^6). Figure 3 shows the results for the soil source simulation. The largest cylindrical soil source selected in this study was radius = 5 m and thickness = 0.6 m. So in the MCNP simulation the center of cylindrical soil source is (50.00 cm, −200.10 cm, 31.65 cm). The natural activities of U/Ra, ^{232}Th, and ^{40}K in the soil model were 2.36×10^6 Bq, 3.27×10^6 Bq, and 3.75×10^7 Bq, respectively.

The main source of radioactivity in air is Rn. The main sources of Rn are ^{222}Rn, ^{220}Rn, and ^{219}Rn. Since the half-lives of the latter two are only 55.6 s and 3.82 s, only a very small part of ^{220}Rn and ^{219}Rn produced in the earth's crust can be released into the environment. Even if they are released into the environment, they decay in a very short time. Therefore, only the effect of ^{222}Rn

2022 JINST 17 P09044

Table 1. Photopeak energies and intensities of soil background source model [18].

Nuclide	Energy (MeV)	Intensities (%)	Nuclide	Energy (MeV)	Intensities (%)	Nuclide	Energy (MeV)	Intensities (%)
^{234}Th	0.063	3.8	^{214}Bi	1.729	2.9	^{228}Ac	0.911	25.8
^{226}Ra	0.186	3.6		1.764	15.3		0.969	15.8
^{214}Pb	0.242	7.26		1.847	2.0	^{224}Ra	0.241	3.9
	0.295	18.5		2.204	4.9	^{212}Pb	0.239	43.6
	0.352	35.7	^{212}Bi	0.727	6.7		0.300	3.3
^{214}Bi	0.609	45.4	^{210}Pb	0.047	4.0	^{208}Ti	0.277	2.5
	0.768	4.9	^{228}Ac	0.129	2.4		0.511	7.8
	0.935	3.1		0.209	4.0		0.583	30.5
	1.120	14.9		0.270	3.5		0.860	4.3
	1.238	5.8		0.328	3.0		2.615	35.6
	1.378	4.0		0.338	11.3	^{40}K	1.461	10.7
	1.408	2.8		0.674	2.1			
	1.509	2.2		0.795	4.3			

Table 2. The median values of the distributions of the average top thirteen elements from the world soil series.

Element	O	Si	Al	Fe	C	Ca	K	Na	Mg	Ti	N	S	P
Weight (%)	49.0	33.0	7.10	3.80	2.00	1.37	1.36	0.63	0.63	0.46	0.10	0.09	0.08

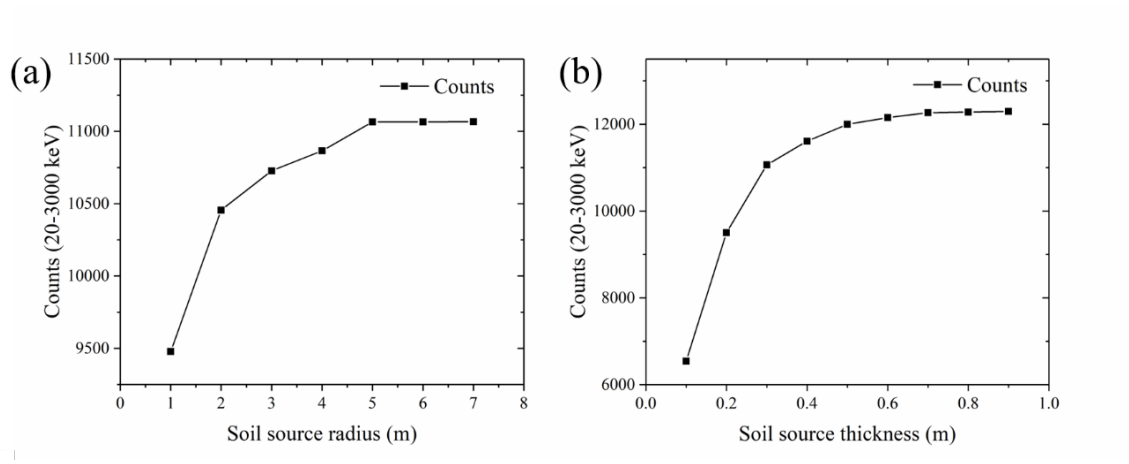

Figure 3. MCNP simulation results of cylindrical soil source: (a) with different radius (thickness = 0.3 m), (b) with different thicknesses (radius = 5 m).

(radioactive period of 3.8 days) on the detector is studied. The Rn activity concentration used in the Monte Carlo simulation was 13.83 Bq/m^3, and the data came from the China Institute of Radiation Protection (CIRP) [20]. The air model was a cube model of 25 m, in which the natural activity of ^{222}Rn was 2.16×10^5 Bq. And the energy of the ^{222}Rn nuclide with the total photon intensities greater than 2% in the series decay was used, which is consistent with the above principle. The specific representative energy and corresponding photon intensities are shown in table 3.

2022 JINST 17 P09044

Table 3. Photopeak energies and intensities of air background source model [18].

Nuclide	Energy (MeV)	Intensities (%)	Nuclide	Energy (MeV)	Intensities (%)
^{214}Pb	0.242	7.26	^{214}Bi	1.378	4.0
	0.295	18.5		1.408	2.8
	0.352	35.7		1.509	2.2
^{214}Bi	0.609	45.4		1.729	2.9
	0.768	4.9		1.764	15.3
	0.935	3.1		1.847	2.0
	1.120	14.9		2.204	4.9
	1.238	5.8	^{210}Pb	0.047	4.0

Soil source and air source constitute the background environmental sourced of VM-WBC. Without shielding, the simulated background energy spectrum (10 min) of soil source and air source is shown in figure 4. The 609 keV full-energy peak of ^{214}Bi in the ^{238}U decay chain, the 1461 keV full-energy peak of ^{40}K, and the 2615 keV full-energy peak of ^{208}Tl in the ^{232}Th decay chain were marked in the energy spectrum. The energy spectrum counts caused by the soil sources were about 100 times that of air sources, so the background energy spectrum of the whole-body counter was mainly contributed by soil sources.

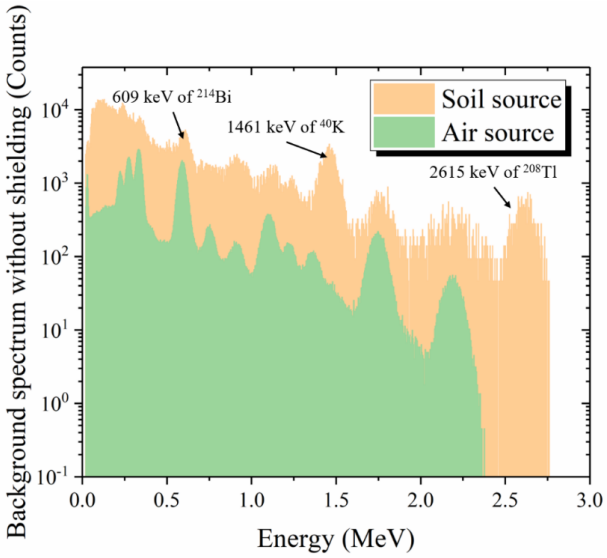

Figure 4. 10-min simulated energy spectra of soil source and air source without shielding.

The simulated energy spectrum and the experiment energy spectrum with a $4'' \times 4'' \times 16''$ NaI(Tl) detector are shown in figure 5. The experimental and simulated energy spectra were basically consistent, verifying the simulation settings' accuracy. Experiment background counts from 0–200 keV were more than the simulation part because the real environment contains more low-energy particles.

2022 JINST 17 P09044

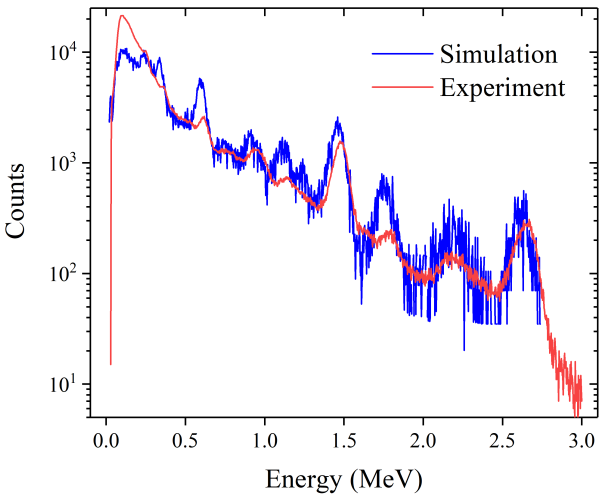

Figure 5. Comparison of experimental and simulated energy spectra in 10 min.

2.1.3 Modeling of the detector shielding structure

Two shielding structures were designed, and their schematic diagrams are shown in figure 6. During a nuclear accident, the activity of radionuclides entering the human body is low. To obtain accurate measurement results, VM-WBC requires a measurement environment with low activity levels. Since materials such as lead and steel are inherently radioactive, low activity materials are needed to minimize background counts. In fact, the current mainstream commercial WBC. For example, Mirion Technologies' FASTSCAN^{TM} 2250 High-Throughput Whole Body Counter, and ORTEC's StandFAST II Stand Up Whole Body Counter all use low-background shielding materials [8, 9]. Therefore, in this study we also use low-background materials. The shielding structure design of VM-WBC uses shadow shielding to minimize the background [21]. Figure 6(a) shows a steel structure. The main body of the steel structure is all composed of low background steel. Figure 6(b) shows a lead structure. The outermost layer of the lead shielding structure was made of 1 cm low background steel. The middle layer is low background lead. The inner layer was composed of 0.3 cm low background copper, which can support the inner layer of the lead structure and shield detectors from the radioactive background of lead itself as well as the secondary fluorescence X-rays produced in lead by environmental radiation (for example, the K_α photons with an energy of about 73, 75, 85 and 87 keV). In these two structures, there is no shielding material on the upper surfaces of detectors. This article illustrated the internal construction through two cross-sectional views of a more complex lead structure. Figure 6(c) with the long side of the detector as the cross-section, and figure 6(d) with the short side of the detector as the cross-section. Figure 6(c) shows the internal structure of the NaI(Tl) scintillator detector, including PMT, aluminum housing, light guide material SiO_2, reflector material MgO, and NaI crystal. The sidewall and bottom wall thickness locations that needed to be explored were indicated by red lines. Compared with the upper surface of the detector, the surrounding shielding material was extended upwards by 1.4 cm (figure 6(c)), which can take into account the measurement angle requirements and shielding requirements.

2022 JINST 17 P09044

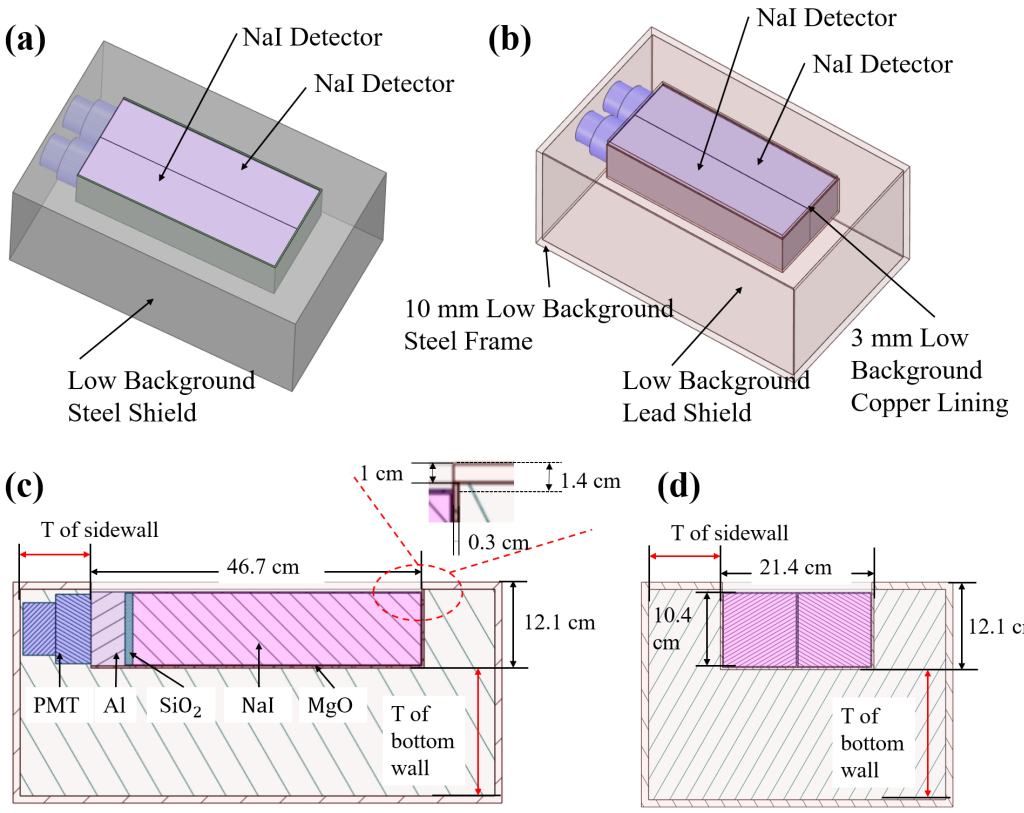

Figure 6. Shielding design of whole-body counter: (a) steel structure; (b) lead structure; (c) cross-section of the lead structure, with the long side of the detector as the cross-section; and (d) cross-sectional view of the lead structure, with the short side of the detector as the cross-section.

Figure 7 illustrates the comparison of the background energy spectrum with the optimal shielding structure and without shielding. In figure 5, the 609 keV all-energy peak of ^{214}Bi, the 1461 keV full-energy peak of ^{40}K, and the 2614 keV full-energy peak of ^{208}Tl were also marked. The shielding structure greatly reduced the background counts, especially in the high-energy region (1–3 MeV). In the energy spectrum accompanying the shielding structure, the counts in the low-energy band (0–1 MeV) mainly come from the bremsstrahlung generated by the background radiation in the shielding structure and the secondary photons generated by the scattering.

2.2 MDA calculation results of two shielding structures

MDA is one of the most important parameters of the WBC. If the activity of a nuclide is higher than its MDA value, it can be reliably measured by the detection system [22]. According to the requirements of personal internal exposure detection, the MDA of the two nuclides of ^{60}Co and ^{137}Cs in the whole-body counter should be less than 50 Bq (ICRP 78) [11]. During the simulation,

2022 JINST 17 P09044

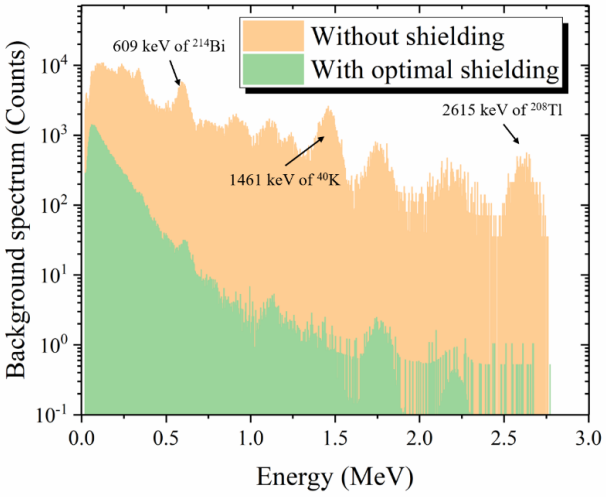

Figure 7. Background spectrum for without shielded and with optimally shielded structures in 10-min MCNP simulation.

the MDA of the whole-body counter measurement system can be expressed as [23]:

$$\mathrm{MDA} = \frac{L_D}{\varepsilon_m p T_L} \tag{2.1}$$

$$L_D = k^2 + 2k\sigma_0 = 2.71 + 4.65\sqrt{B} \tag{2.2}$$

Where T_L [s] is the measurement live time (the time 10 min is assumed in the present study); p is the emission probability of gamma rays; ε_m is the full-energy peak detection efficiency; L_D (with a confidence level of 95%) is the minimum detectable limit for the Region of Interest (ROI); k is the one-sided confidence factor; σ_0 is the standard deviation of the distribution ($\sigma_0^2 = 2B$); and B is the number of background events in the ROI of the peak analyzed in 10 min. The width of the ROI is related to the FWHM(E) function of each detector:

$$n = n_E = K \times \mathrm{FWHM}(E) \tag{2.3}$$

where K is the proportionality constant for the desired peak coverage. FWHM(E) is determined by the detector. Such as, $K = 2.548$ represents 99.73% peak area coverage, $n_{662} = 53\,keV$, $n_{1173} = 96\,keV$, $n_{1332} = 108.9\,keV$. The key to reduce the MDA value is to increase the counting efficiency ε_m of the detector and reduce the background of the peak area B.

During the simulation, two nuclides, ^{60}Co and ^{137}Cs, were uniformly distributed inside the ANSI-man and ANSI-female phantoms. The MDA value of ^{60}Co and ^{137}Cs in ANSI-Man and ANSI-Female were calculated by changing the thickness of the bottom wall of the detector. The effect of changes in sidewall thickness on MDA is shown in figure 8. When the sidewall thicknesses of the two structures are 15 cm and 10 cm, respectively, the effect of increasing wall thickness to the reduction of MDA is no more significant. Therefore, the thickness of the sidewall in the steel structure was 15 cm, and the thickness of sidewall in the lead structure was 10 cm.

2022 JINST 17 P09044

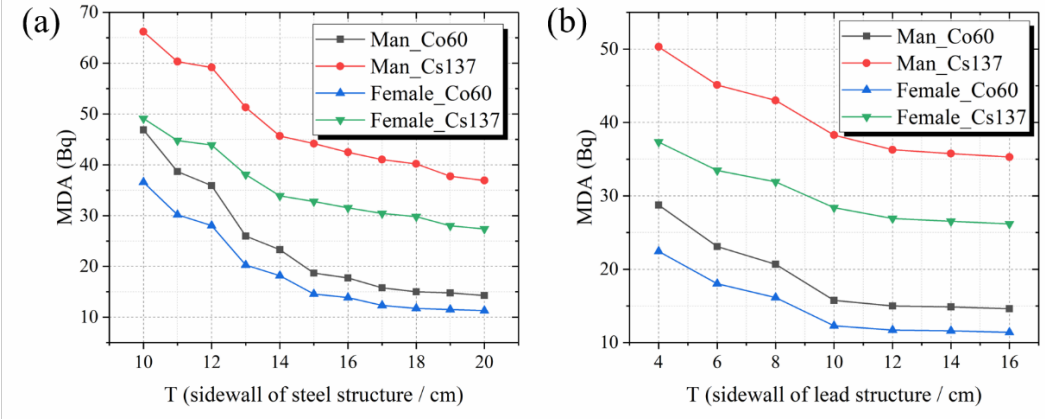

Figure 8. Effects of variation in sidewall thickness on system MDA: (a) MDA of steel structure system when the bottom wall was 25 cm. (b) MDA of lead structure system when the bottom wall was 18 cm.

The effect of changes of the bottom wall thickness on MDA is shown in figure 9. The MDA of both structures decreases with the increase of the thickness at the bottom of the detector. However, under the condition of basically the same weight, as shown by the green dotted line in figure 9, the overall MDA of the lead structure is smaller than that of the steel structure. Therefore, the lead structure was chosen. And comparing the simulation results of the side wall and bottom wall of the two shielding structures, it can be found that the change of the bottom wall thickness has a greater impact than the change of the side wall thickness. Although background radiation can also be detected at the bottom and sides of the NaI crystal, the bottom of the crystal is more affected by the background radiation.

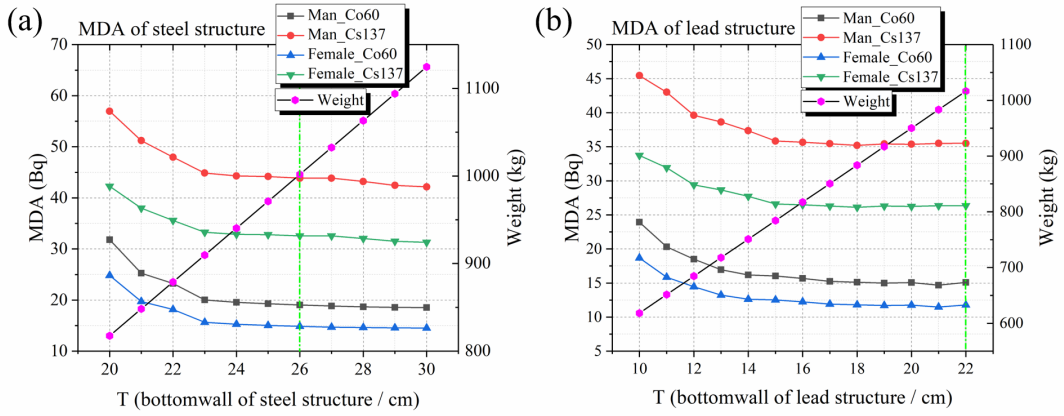

Figure 9. Effects of variation in bottom wall thickness on system MDA: (a) MDA of steel structure system when the sidewall was 15 cm. (b) MDA of lead structure system when the sidewall was 10 cm.

In the Monte Carlo model, human phantoms of different body types represent different sizes of sources. As shown in figure 9, the calculated MDA of the male phantom is larger than that of the female phantom. This is due to the larger size of the male phantom (leading to a lower geometric

2022 JINST 17 P09044

efficiency) and to the greater self-absorption effect. Structures with a thickness of 10–21 cm at the bottom meet the design requirements (MDA < 50 Bq, weight < 1000 kg). Considering the shielding performance and weight limitations, the bottom thickness of 15 cm was selected as a good compromise. The simulation calculation results are shown in table 4.

Table 4. Simulation results for the bottom wall thickness of the passive shield $T = 15$ cm.

Phantom	MDA_^{137}Cs (Bq)	MDA_^{60}Co (Bq)	Weight of shielding structure (kg)
ANSI-Man	35.8	16.0	784
ANSI-Female	26.6	12.5	784

3 Simulations of the VM-WBC detection efficiency

3.1 Efficiency calibration based on different reference phantoms

Phantoms should be used for counting efficiency calibration prior to the whole-body counter application. In practical applications, the counting efficiency is affected by the size of the human body. In the application of internal irradiation efficiency calibration, the most widely used phantom is the Bottle Manikin Absorption (BOMAB) phantom, developed by Bush in 1949 [24]. It consists of ten polyethylene parts representing different parts of the body and can be filled with a radioactive solution for calibration. BOMAB phantoms of different sizes can be used to calibrate whole-body counters [25].

Using only reference phantom data in calibration can lead to serious errors [26]. This study aims to use two sets of BOMAB phantoms for simulation efficiency calibration. The first is the ANSI series of BOMAB phantoms, representing 4-year-old, 10-year-old, adult female, adult male, and 95th percentile male phantoms [12]. In addition, this study constructed a set of radiation computing phantoms with Chinese reference physiological characteristics representing different age groups [27, 28]. There are 5-year-old, 10-year-old, 15-year-old male, 15-year-old female, adult female, and adult male phantoms with Chinese reference physiological characteristics. The basic data of the two sets of phantoms are shown in table 5 and include height, weight, and Body Build Index (BBI). BBI is defined as $(W/H)^{1/2}$, where W and H are the patient's weight and height, respectively.

The ray energy emitted from 10 nuclides was used in this paper, as shown in table 6. The radionuclides are uniformly distributed inside the BOMAB phantom.

3.2 Results of detector efficiency simulation

Figure 10 shows the simulation results of two different types of reference BOMAB phantoms. The counting efficiency of the phantom as a function of photon energy and BBI.

The counting efficiency decreases with increasing BBI because of a larger attenuation in the phantom and hence a smaller number of photons reaching the detector. These results suggest that BBI can be used as a key parameter for the calibration of phantoms of different sizes.

In this study, using the function fitting tool tableCurve 3D v4.0, the above data were fitted to obtain a mathematical function of counting efficiency as a function of energy and BBI, given by the

2022 JINST 17 P09044

Table 5. Two groups of reference man body parameters.

Mode	Age (years)	Height (cm)	Weight (kg)	BBI $(W/H)^{1/2}$
ANSI BOMAB Phantoms	4	106	17.6	0.407
	10	143	33.8	0.486
	Adult Female	162	57.5	0.596
	Adult Male	176	74.2	0.649
	95% Male	188	103.1	0.741
Chinese reference man	5	110	18.6	0.411
	10	139	35.0	0.502
	15 Female	158	49.7	0.561
	Adult Female	158	55.0	0.590
	15 Male	168	58.0	0.588
	Adult Male	170	70.0	0.642

Table 6. Radionuclides used for calibration and their representative energy levels.

Nuclide	Energy (keV)	Nuclide	Energy (keV)	Nuclide	Energy (keV)
^{109}Cd	88	^{113}Sn	391	^{88}Y	898
^{57}Co	122	^{54}Mn	468		1836
^{139}Ce	165	^{137}Cs	662	^{60}Co	1173
^{203}Hg	279	^{40}K	1461		1332

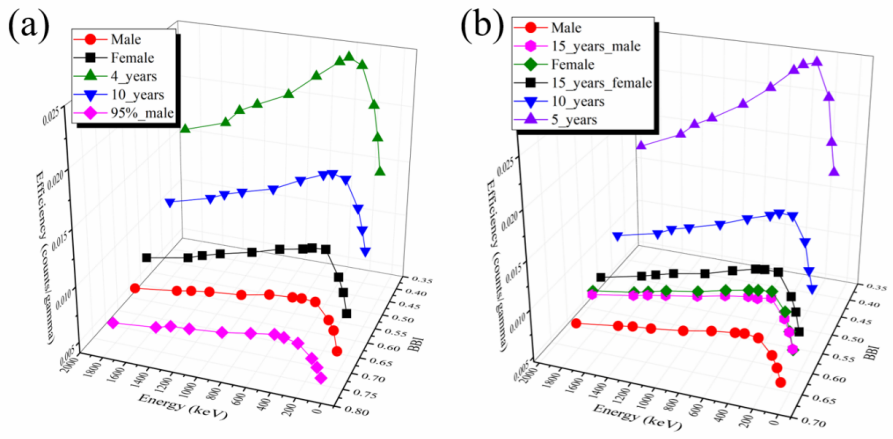

Figure 10. Simulated counting efficiency as a function of photon energy and BBI: (a) fitting results for ANSI BOMAB phantoms and (b) fitting results for Chinese reference man.

following equations:

$$z' = \frac{a + b\ln x + c\ln y + d(\ln y)^2 + e(\ln y)^3}{1 + f\ln x + g(\ln x)^2 + h\ln y} \tag{3.1}$$

$$z'' = \frac{i + j\ln x + k\ln y + l(\ln y)^2 + m(\ln y)^3}{1 + n\ln x + o(\ln x)^2 + p(\ln x)^3 + q\ln y} \tag{3.2}$$

2022 JINST 17 P09044

Where equation (3.1) is the fitting result of the ANSI phantom, and equation (3.2) is the fitting result of the Chinese reference person, z' and z'' are the corresponding counting efficiencies, x is photon energy, y is BBI, and $a \sim q$ are regression coefficients. The obtained parameters are shown in table 7.

Table 7. Fitting parameter values.

Model	Parameter	Value	Parameter	Value
ANSI BOMAB phantoms	a	−0.00050	g	0.02583
	b	0.00009	*h*	−0.01280
	c	−0.00324	Correlation coefficient	0.99059
	d	−0.00514	Standard error	0.00056
	e	−0.00506	F-value*	781
	f	−0.30673	-	-
Chinese reference man	i	−0.00102	o	0.06125
	j	0.00006	*p*	0.00278
	k	−0.00488	*q*	0.00249
	l	−0.00803	Correlation coefficient	0.99680
	m	−0.00566	Standard error	0.00035
	n	−0.42708	F-value	2420

* F-value indicates the significance of the entire fitting equation. The larger the F-value the more significant the equation and the better the fit.

A phantom (H = 161 cm, W = 49.67 kg) representing 5% of males was used to verify the above two fitting functions [29], and the energy used was 661.7 keV, 1173.2 keV, and 1332.5 keV. The deviation of the relative counting efficiency calculation is shown in table 8. The relative differences between the calculation results with the two formulas and the Monte Carlo simulation results are all within 5%. In particular, the errors come from the calculation results of eq. (3.2) and the Monte Carlo simulation results are within ±1%.

Table 8. Relative difference between the counting efficiency obtained by Monte Carlo simulation and that calculated with eq. (3.1) and eq. (3.2).

Energy (keV)	**Monte Carlo simulation**	**Eq. (3.1) calculation / Deviation value**	**Eq. (3.2) calculation / Deviation value**
661.7	0.01200	0.01195 / 0.48%	0.01210 / −0.79%
1173.2	0.01042	0.01006 / 3.45%	0.01040 / 0.15%
1332.5	0.01003	0.00957 / 4.56%	0.01006 / −0.29%

The simulation results of the Chinese reference phantom are consistent with the results using the ANSI phantom. Moreover, the standard error and deviation value of the eq. (3.2) is smaller than the eq. (3.1). Therefore, eq. (3.2) can be used for efficiency calibration to obtain more accurate results.

3.3 Effects of body positioning uncertainties

The effect of patient position deviations on counting efficiency was also studied. By fixing the scanning interval, the model is moved longitudinally (X-axis) and transversally (Y-axis) by a certain

2022 JINST 17 P09044

distance to form a placement deviation. The schematic diagram is shown in figure 11. The geometric center position of the adult male phantom was set to zero. Given the limited space inside the vehicle, the Y-axis deviations are ±1, ±3, and ±5 cm, and the X-axis deviations are ±1, ±5, and ±10 cm.

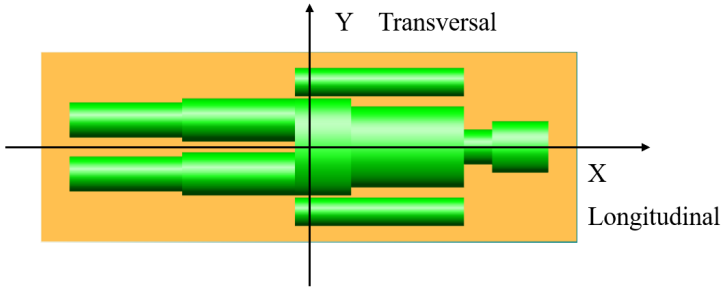

Figure 11. Schematic diagram of patient measurement position deviation.

The simulation results are shown in figure 12, where the deviations of the relative counting efficiency depending on the phantom position are presented. X-axis deviation distance does not cause significant deviation of the detection efficiency. A maximum detection efficiency deviation is 1.6% with an average deviation of 0.9%. The phantom has a relative detection efficiency deviation of −4% at the Y-axis ± 5 cm position with an average deviation of -2.1%.

The deviation value caused by the variation of the phantom position along the X-axis direction is smaller than that caused by the Y-axis. Because when a X-axis deviation occurs, most of the body parts of the human body are still scanned and detected, and only a small area of the head or legs cannot be detected. When a deviation in the Y-axis direction occurs, some parts of the entire human body will not be scanned, which will cause a larger uncertainty. The deviation values formed in these two directions were both within 5%, because the NaI(Tl) detector has a certain detection solid angle, so that the detectable range exceeded the body range of the phantom. In the application of VM-WBC, the measurement uncertainty of counting efficiency due to body positioning is negligible.

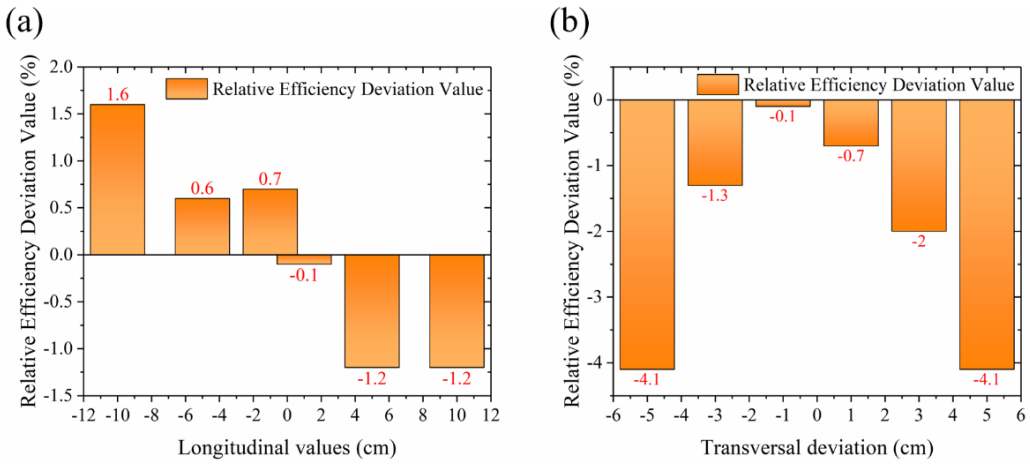

Figure 12. Simulated deviations due to positioning uncertainties: (a) deviations in longitudinal; (b) deviations in transversal.

2022 JINST 17 P09044

4 Conclusions

In this study, Monte Carlo simulation with MCNP computer code was used to design a lightweight shielding structure with theoretical performances complying that meets the ICRP78 requirements [11]. The total mass of the optimal shielding structure obtained by MCNP simulation is about 800 kg, and the MDA values of ^{60}Co and ^{137}Cs are both less than 50 Bq for a 10 min acquisition. The efficiency of the WBC designed in this study was then calculated using the MCNP computer code, and variations of the detection efficiency to gamma-ray quanta emitted from different body sizes phantoms were studied. Differences in patient size (e.g. male, female, children of different ages) can have a significant impact on counting efficiency. In addition, fitting functions of counting efficiency as a function of energy and BBI were obtained. The accuracy of the Chinese reference phantom applied to the efficiency calibration was verified by comparing the result obtained with the fitting functions to MCNP calculations with a phantom that was not used to establish the fit. This study also explored the influence of positioning deviation during patient testing, which is lower than 5% in all studied cases. The results can provide new ideas for the application of WBC and improve the efficiency and speed of internal exposure detection in nuclear accidents.

However, in this paper, the shielding performance and WBC detection efficiency of vehicle-mounted whole-body counter were investigated using simulation means. In the follow-up, the shielding performance verification experiment and efficiency calibration experiment of VM-WBC should be carried out.

Acknowledgments

This work was supported by the Primary Research and Development Plan of Jiangsu Province (Grant No. BE2019727), and the Fundamental Research Funds for the Central Universities (Grant No. NC2022006).

References

[1] O. Kurihara, C. Li, M.A. Lopez, E. Kim, K. Tani, T. Nakano et al., *Experiences of population monitoring using whole-body counters in response to the Fukushima nuclear accident*, *Health Phys.* **115** (2018) 259.

[2] Y. Sekitani, N. Hayashida, I.V. Karevskaya, O.A. Vasilitsova, A. Kozlovsky, M. Omiya et al., *Evaluation of 137Cs body burden in inhabitants of Bryansk Oblast, Russian Federation, where a high incidence of thyroid cancer was observed after the accident at the Chernobyl nuclear power plant*, *Radiat. Protect. Dosim.* **141** (2010) 36.

[3] M. Thieme, E.L. Hunt, K. Konig, A. Schmitt-Hannig and R. Godde, *European whole body counter measurement intercomparison*, *Health Phys.* **74** (1998) 465.

[4] F. Bronson, R. Hayano, B. Oginni, H. Jaderstrom, G. Ilie, S. Yamanaka et al., *Design, development, and initial operation of BabyScan: An in-vivo counter for children around fukushima*, *Nucl. Instrum. Meth. A* **784** (2015) 610.

[5] F.G. Paiva, A.H. de Oliveira, B.M. Mendes, J.R. Pinto, N. do Nascimento A. Filho, B.M. Dantas et al., *Improvement of the WBC calibration of the internal dosimetry laboratory of the CDTN/CNEN using the physical phantom BOMAB and MCNPX code*, *Appl. Radiat. Isot.* **117** (2016) 123.

2022 JINST 17 P09044

[6] B. López, J.N. Amaro, M.L. Ponte and A.C. Fernández, *CIEMAT WBC capabilities for responding in case of nuclear and radiological emergencies*, *Radiat. Phys. Chem.* **176** (2020) 108977.

[7] K. Tani, Y. Igarashi, E. Kim, M. Kowatari, T. Iimoto and O. Kurihara, *Probabilistic analyses of 131i thyroid activity in persons with surface contamination in direct measurement with a standing-type whole-body counter as an emergency response in a radiological incident*, *Radiat. Protect. Dosim.* **194** (2021) 65.

[8] *StandFAST II Stand Up Whole Body Counter, Radionuclide Detection, AMETEK ORTEC*, https://www.ortec-online.com/products/radiochemistry-health-physics-research-industrial/health-physics-systems/body-counting-systems/standfast-ii, 2022.

[9] *2250 FASTSCAN^{TM} High-Throughput Whole Body Counter*, https://www.mirion.com/products/2250-fastscan-high-throughput-whole-body-counter.

[10] *New Daily Van, Iveco (China) — Iveco Imported Vehicles, Imported Iveco*, https://www.iveco.com.cn/products/new_daily_van/, 2022.

[11] ICRP, *Individual Monitoring for Internal Exposure of Workers*, *ICRP Publication* **78**, *Ann. ICRP* **27** (3–4), 1997.

[12] A.N.S. Institute, *ANSI/HPS N13.35-2009 Specifications for the Bottle Manikin Absorption Phantom*, 2009.

[13] J. Bento, S. Barros, P. Teles, M. Neves, I. Goncalves, J. Corisco et al., *Monte carlo simulation of the movement and detection efficiency of a whole-body counting system using a BOMAB phantom*, *Radiat. Protect. Dosim.* **148** (2011) 403.

[14] M. Park, H.S. Kim, J. Yoo, C.H. Kim, W.I. Jang and S. Park, *Virtual calibration of whole-body counters to consider the size dependency of counting efficiency using Monte Carlo simulations*, *Nucl. Eng. Technol.* **53** (2021) 4122.

[15] W.C. Zhao Fuxiang, *Investgation of Natural Radionuclide Contents in Soil in Jiangsu Province*, *Radiat. Prot.* **6** (1992) 452.

[16] J. Wallace, *Monte carlo modelling of large scale NORM sources using MCNP*, *J. Environ. Radioact.* **126** (2013) 55.

[17] G. Gilmore, *Practical Gamma-ray Spectroscopy*, John Wiley & Sons, Ltd (2008).

[18] *Livechart — Table of Nuclides — Nuclear structure and decay data*, https://www-nds.iaea.org/relnsd/vcharthtml/VChartHTML.html, 2022.

[19] L. Wielopolski and O. Doron, *Nuclear spectroscopy for in situ soil elemental analysis: Monte Carlo simulations*, *Appl. Radiat. Isot.* **70** (2012) 1085.

[20] S. Li, *Indoor and Outdoor Radon Lev els and Dose Estimation in Som e Areas of China*, *Radiat. Prot. Bull.* **6** (1999) 2.

[21] M. Manohari, P. Sugumar, R. Deepu, R. Mathiyarasu and B. Venkatraman, *Comparison of indian BOMAB and ICRP voxel phantom for calibration of shadow shield whole body counter*, *Appl. Radiat. Isot.* **180** (2022) 110020.

[22] J. Bento, P. Teles, L. Silva, P. Nogueira, M. Neves and P. Vaz, *Performance parameters of a whole body counter*, *Radiat. Meas.* **45** (2010) 190.

[23] X.-B. Tang et al., *Simulated minimum detectable activity concentration (MDAC) for a real-time UAV airborne radioactivity monitoring system with HPGe and LaBr3 detectors*, *Radiat. Meas.* **85** (2016) 126.

2022 JINST 17 P09044

[24] F. Bush, *The integral dose received from a uniformly distributed radioactive isotope*, British J. Radiol. **22** (1949) 96.

[25] B. Zhang, M. Mille and X.G. Xu, *An analysis of dependency of counting efficiency on worker anatomy for in vivo measurements: whole-body counting*, Phys. Med. Biol. **53** (2008) 3463.

[26] Y. Chen, R. Qiu, C. Li, Z. Wu and J. Li, *Construction of chinese adult male phantom library and its application in the virtual calibration of in vivo measurement*, Phys. Med. Biol. **61** (2016) 2124.

[27] W. Jixian and C. Rusong, *Data of Anatomical Physiological and Metabolic Characteristics for Chinese Reference Man*, (2002).

[28] Institute of Radiation Medicine Chinese Academy of Medical Sciences, *Reference individuals for use in radiation protection Part I: Physique parameters*, National standards of the people's Republic of China, (2007).

[29] G.H. Kramer, L.C. Burns and S. Guerriere, *Monte Carlo simulation of a scanning detector whole body counter and the effect of BOMAB phantom size on the calibration*, Health Phys. **83** (2002) 526.

2022 JINST 17 P09044